PNAS RESEARCH ARTICLE | PHYSICS OPEN ACCESS

Resilient $j = 3/2$ superconductivity in topological semimetal YPtBi

Prathum Saraf[a], Nicholas A. Crombie[a], Rahul Sharma[a], Jared Z. Dans[a], Danila Sokratov[a], Carsyn L. Mueller[a], Ram Kumar[a], Hyunsoo Kim[a,b], Connor Roncaioli[a], Winslow Weiss[a], Arthur Carlton-Jones[a], Peter Y. Zavalij[c], David Graf[d], Chandra Shekhar[e], Steven M. Anlage[a], Claudia Felser[e,f,1], and Johnpierre Paglione[a,f,1]

Affiliations are included on p. 7.

Contributed by Claudia Felser; received June 11, 2026; accepted October 5, 2026; reviewed by Chris J. Palmstrom and Anne de Visser

Cooper pairing in most of the known fermionic superfluids occurs via spin-1/2 quasiparticle interactions that lead to spin-singlet or spin-triplet pairing. In the topological semimetal YPtBi, strong spin–orbit coupling results in a band inversion between highly symmetric *s*- and *p*-like electronic bands and a degeneracy at the Γ point that ensures the manifold of $j = 3/2$ quasiparticle states thrive near the Fermi level, where superconducting pairing occurs. Here we study the effects of magnetic and nonmagnetic disorder and carrier density on this exotic superconducting pairing state. By varying levels of disorder and carrier densities by nearly two and three orders of magnitude, respectively, we show that the superconducting critical temperature of YPtBi has a remarkable robustness, with little variation across this span. Our results suggest that superconductivity in YPtBi may reside in a regime where phase stiffness, rather than pair formation, governs the transition temperature. The insensitivity of Cooper pairing to dramatic changes in quasiparticle environment in a $j = 3/2$ superconductor highlights a form of protection realized in topological high-spin superconductors.

superconductivity | topological semimetal | high-spin pairing

Significance

Superconductivity is typically understood to depend on the density of electronic states at the Fermi level and is disrupted by disorder or magnetism. Here, we show that the half-Heusler semimetal YPtBi defies these expectations. Across wide variations in carrier density, disorder, and in the presence of magnetic doping, the superconducting transition temperature remains unchanged. By combining transport and quantum oscillation, we demonstrate that superconductivity in this system might be governed not by conventional pairing at the Fermi surface, but by phase coherence in a dilute, strongly spin–orbit-coupled electronic system. These findings establish YPtBi as a platform for superconductivity beyond the conventional paradigm.

The topological semimetal YPtBi is a prominent member of the half-Heusler family known to host inverted bands, strong spin–orbit coupling, and unconventional superconductivity (1–3). Superconductivity below 1 K was first reported in YPtBi despite an exceptionally low carrier density of only $n \sim 10^{18}$ cm^{-3} (4–6), far below that expected for conventional electron–phonon pairing (7). Similar to the case of dilute superconductor $SrTiO_3$, which has a similar carrier density (albeit with much lower T_c) (8), the survival of superconductivity in this limit is in contrast to basic expectations for a conventional superconductor where theory would predict vanishingly small transition temperatures. However in YPtBi, strong spin–orbit coupling and the inversion of the Γ_6 and Γ_8 bands stabilize quasiparticles with dominant $j = 3/2$ character near the Fermi level (6, 9), allowing a richer manifold of pairing channels, including singlet ($J = 0$), triplet ($J = 1$), quintet ($J = 2$) and septet ($J = 3$) states (5, 9–11). Together with evidence of nodal excitations from penetration depth measurements (5, 12), the possibility of unconventional topological superconductivity in this otherwise unassuming material has spurred great interest (10, 13–26).

A central unresolved question is how such a low-density $j = 3/2$ superconducting state responds to perturbations that strongly modify the normal state electronic structure. In conventional superconductors, disorder and carrier density tuning primarily affect superconductivity through changes in the density of states or pair-breaking. Here, we investigate the response of YPtBi to disorder, hole doping, and magnetic substitution using electrical transport, Hall effect, and quantum oscillation measurements. Despite dramatic changes in scattering, conductivity, and Fermi surface properties, superconductivity remains remarkably robust. This resilience suggests that superconductivity in YPtBi is not governed solely by conventional amplitude-based pairing considerations, but instead may derive substantial stability from the phase stiffness and topology of the underlying superconducting state.

To systematically investigate the effects of disorder and doping on both the superconductivity and normal state electronic properties of YPtBi, we compare the response of electrical transport, quantum oscillations, and Hall effect measurements in five types of samples: conventional YPtBi, ultra-high purity YPtBi, chemically disordered YPtBi, hole-doped (Y,Ca)PtBi and magnetically-substituted (Y,Nd)PtBi.

Author contributions: C.F. and J.P. designed research; P.S., N.A.C., R.S., J.Z.D., D.S., C.L.M., R.K., H.K., W.W., A.C.-J., P.Y.Z., D.G., C.S., S.M.A., and J.P. performed research; P.S., N.A.C., R.S., J.Z.D., D.S., C.L.M., R.K., H.K., C.R., W.W., P.Y.Z., D.G., C.S., S.M.A., and J.P. analyzed data; and P.S., N.A.C., R.S., J.Z.D., D.S., C.L.M., R.K., H.K., W.W., D.G., C.S., C.F., and J.P. wrote the paper.

Reviewers: C.J.P., University of California, Santa Barbara; and A.d.V., Amsterdam University.

The authors declare no competing interest.

Copyright © 2026 the Author(s). Published by PNAS. This open access article is distributed under Creative Commons Attribution License 4.0 (CC BY).

[1]To whom correspondence may be addressed. Email: claudia.felser@cpfs.mpg.de or paglione@umd.edu.

This article contains supporting information online at https://www.pnas.org/lookup/suppl/doi:10.1073/pnas.2620879123/-/DCSupplemental.

Published November 17, 2026.

Downloaded from https://www.pnas.org by UNIVERSITY OF MARYLAND; MCKELDIN LIBRARY on November 17, 2026 from IP address 129.2.89.183.

These representative cases induce a remarkably wide span of responses in elastic scattering rate (resistivity) and carrier density, while retaining the same character of $j = 3/2$ Fermi surface, and the lack of sensitivity to these perturbations in the superconductivity of YPtBi points to an unique nature of pairing in this system.

Fig. 1*A* presents representative temperature-dependent resistivity measurements from 300 K to 2 K for all four categories of samples. Normal- and high-purity YPtBi,(Y,Nd)PtBi and disordered YPtBi all exhibit nonmetallic behavior characterized by increasing resistivity on cooling, consistent with prior reports (4). In contrast, Ca-doped samples show metallic behavior consistent with the expectation of an increased carrier density, which will be elaborated on below. To understand the degree of metallicity, we extracted the inverse residual resistivity ratio (1/RRR), defined as $1/RRR = \rho(2\,K)/\rho(300\,K)$. The high purity, (Y,Nd)PtBi and disordered samples exhibit significantly larger values of 1/RRR compared to standard YPtBi, suggesting either increased scattering, lowered carrier density, or a combination of both. For instance, in disordered samples, the inclusion of Au during the growth process introduces vacancies and site disorder thought to increase scattering, whereas the high purity YPtBi material is thought to have the lowest carrier density due to reduced impurity doping effects. However, to quantify and segregate these effects, we have performed both Hall effect and quantum oscillations experiments to directly probe the carrier densities. Fig. 1*B* shows the Hall resistivity ρ_{xy} as function of magnetic field at 2 K for all sample types. Across all samples $\rho_{xy}(H)$ is approximately linear as expected for the near-spherical single-band structure of YPtBi (6), allowing us to extract the Hall coefficient $R_H = R_{xy}t/\mu_0 H$ from the slope, where t is the sample thickness. Using the relation $R_H = 1/ne$, we estimate the carrier density n. Standard, high purity, and disordered samples show only minor variations in slope, suggesting slight changes in carrier density. However, the Ca doped samples exhibit a significantly smaller slope corresponding to a substantial enhancement in carrier concentration. This result confirms that Ca substitution for Y acts as a strong hole donor, as expected by its divalent oxidation state.

To examine sample variability, we measured multiple crystals of each type and compiled statistics on transport parameters. Fig. 1*C* summarizes the residual resistivity $\rho_0 = \rho(2\,K)$ and 1/RRR of the samples. Both the disordered and high purity samples consistently show a higher ρ_0 and 1/RRR compared to standard YPtBi. This confirms that the inclusion of Au in the synthesis process indeed introduces disorder into the lattice, enhancing low temperature scattering, while the elevated resistivity and 1/RRR observed in high-purity sample can be

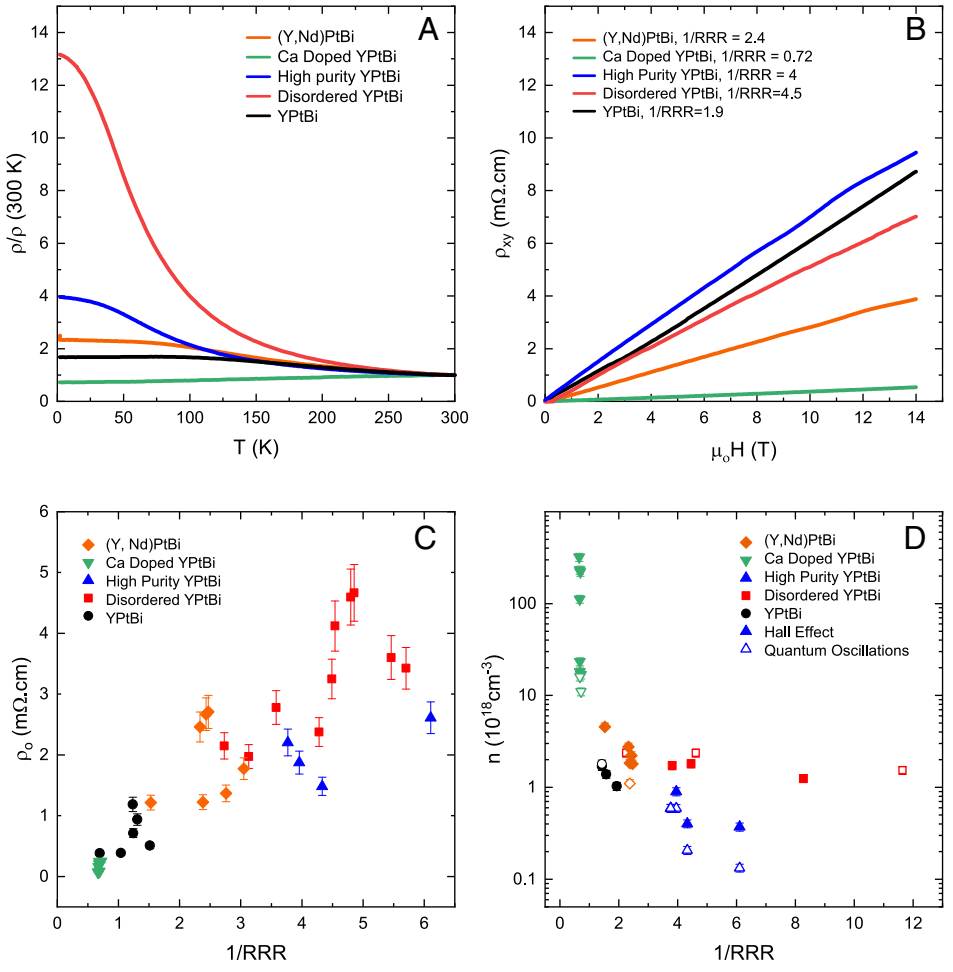


Fig. 1. Variation of transport behavior of YPtBi with disorder, purity, and charge doping. (*A* and *B*) Normalized resistivity and Hall resistivity of the various types of YPtBi grown respectively. Panel (*A*) shows data for $Y_{0.997}Ca_{0.003}PtBi$ and $Y_{0.52}Nd_{0.48}PtBi$, while panel (*B*) shows data for $Y_{0.991}Ca_{0.009}PtBi$ and $Y_{0.80}Nd_{0.20}PtBi$. (*C*) Plot of 1/RRR vs. residual resistivity indicating a change in the residual resistivity in the samples as opposed to room temperature resistivity. (*D*) Carrier density of various samples as a function of 1/RRR. Filled symbols are quantities measured with Hall and open symbols are measured with quantum oscillations.

Downloaded from https://www.pnas.org by UNIVERSITY OF MARYLAND; MCKELDIN LIBRARY on November 17, 2026 from IP address 129.2.89.183.

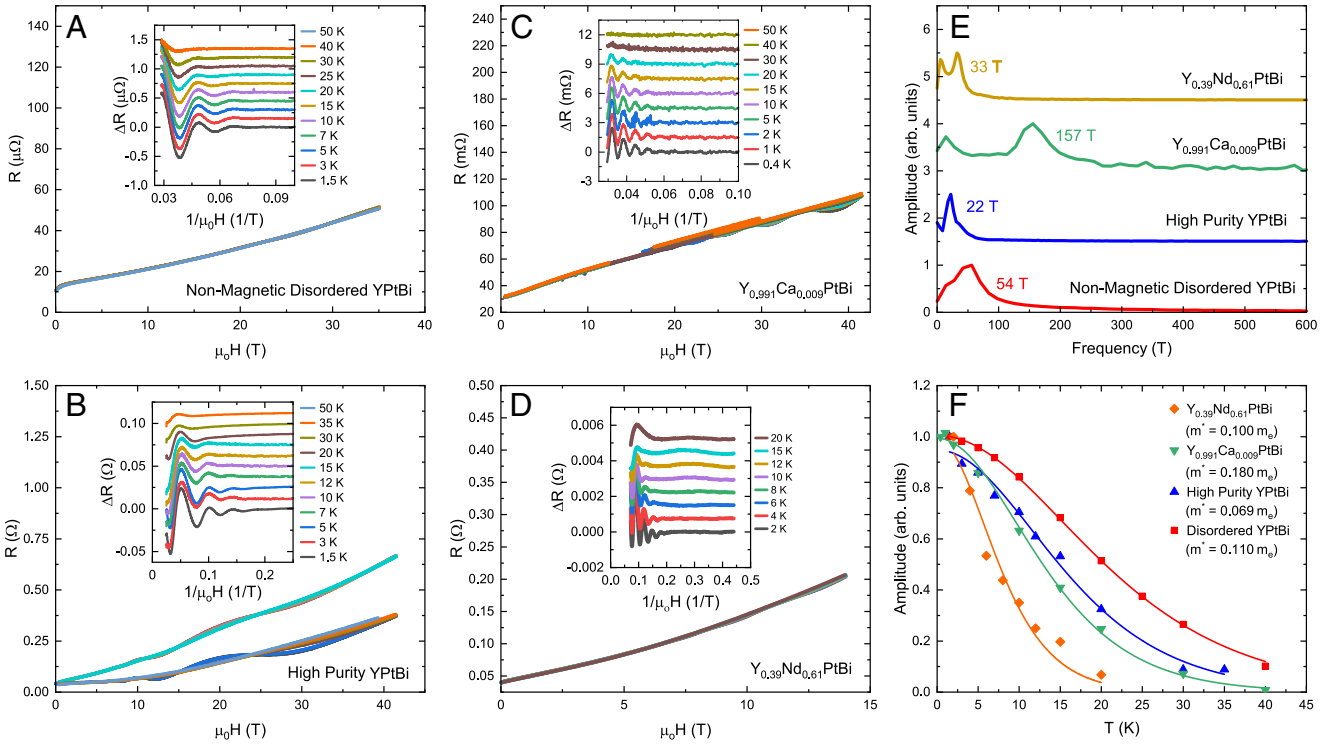


Fig. 2. Quantum oscillations in chemically tuned YPtBi. (*A–D*) Raw data of resistance vs. magnetic field of disordered, high purity, Ca doped samples and (Y,Nd)PtBi respectively. *Inset* shows subtracted resistance curves offset to show the oscillations more clearly. (*E*) Fast Fourier transform of the oscillations showing changes in frequency of the four types of YPtBi. (*F*) Lifshitz–Kosevich fits of the temperature dependence of the amplitude of oscillations which is used to extract the effective mass. Magnetic field for all measurements was perpendicular to the current.

attributed to a lowered carrier density. Fig. 1*D* further illustrates this by plotting carrier density as a function of 1/RRR. The disordered and (Y,Nd)PtBi samples have a similar carrier density ($n_{\text{disordered}} \approx 1.84 \times 10^{18}\,\text{cm}^{-3}$ and $n_{\text{(Y,Nd)PtBi}} \approx 2.63 \times 10^{18}\,\text{cm}^{-3}$) to YPtBi [$n_{\text{YPtBi}} \approx 2 \times 10^{18}\,\text{cm}^{-3}$ (4)], as confirmed by both Hall and quantum oscillation measurements. In contrast, high purity samples show a significantly reduced carrier density ($n_{\text{high purity}} \approx 0.7 \times 10^{18}\,\text{cm}^{-3}$), indicating that the purer raw materials suppress extrinsic doping and bring the Fermi level closer to the band touching point. Ca-doped samples, however, display a wide range of higher carrier concentrations ranging from $n \approx 16 \times 10^{18}$ to $n \approx 320 \times 10^{18}\,\text{cm}^{-3}$, up to two orders of magnitude larger than in YPtBi. These findings confirm that Ca doping increases the number of charge carriers.

Quantum oscillations are a direct, sensitive probe of the Fermi surface and the effective mass of the charge carriers. In standard YPtBi, clear quantum oscillations have been observed at fields below 14 T (5). However, increased impurity scattering in the disordered and Ca-doped samples leads to Dingle damping of the oscillation amplitude (27), making oscillations undetectable up to the same field range. To overcome this limitation we conducted high-field magnetoresistance measurements up to 41.5 T. Fig. 2 *A–D* display the raw magnetoresistance for the high purity, disordered, (Y,Ca)PtBi and (Y,Nd)PtBi samples respectively. Clear Shubnikov de Haas (SdH) oscillations are visible in the high purity samples, with oscillations persisting up to 40 K. The fast Fourier transform (FFT) of this data, shown in Fig. 2*E*, reveals a dominant frequency of $F \approx 22$ T, significantly lower than that of standard YPtBi ($F \approx 51$ T). The temperature dependence of the FFT amplitude shown in Fig. 2*F* fits well to the Lifshitz–Kosevich (LK) expression (27) yielding an effective mass of $m^* = 0.069m_e$ which is notably lighter than that of YPtBi ($m^* = 0.11m_e$). These results are consistent with a smaller Fermi surface and a lower Fermi energy.

Fig. 2*A* presents the weaker quantum oscillations observed in disordered samples. Although the oscillations are less prominent due to increased scattering, the background-subtracted oscillatory component is indeed periodic in $1/\mu_0 H$, as shown in the *Inset*. The FFT in Fig. 2*E* reveals a peak at $F \approx 54$ T, similar to that of YPtBi. The extracted effective mass is $m^* = 0.11m_e$ matching that of YPtBi. These observations suggest that while disorder suppresses the quantum oscillation amplitude by enhancing scattering, it does not significantly shift the Fermi level or alter the carrier density, consistent with the Hall data described above.

Ca substitution, expected to increase hole carrier density, indeed induces a stark shift in the oscillation frequency. FFT analysis (Fig. 2*F*) reveals a threefold increase in frequency up to ∼157 T, reflecting a substantial increase in the Fermi surface cross-sectional area due to elevated carrier density. The LK fit yields an effective mass of $m^* = 0.18m_e$, indicating a heavier band structure at higher energies, likely associated with doping induced band filling. These results confirm that Ca doping raises the Fermi level significantly, modifying both the carrier density and the effective mass. Quantum oscillations of (Y,Nd)PtBi crystals, shown in Fig. 2*D*, are also evident upon background subtraction, and exhibit a reduced frequency of ∼33 T again consistent with reduced carrier density derived from Hall effect measurements. The measured effective mass $m^* = 0.11m_e$ is similar to that of standard YPtBi.

Finally, the effect of these perturbations on the high angular momentum quasiparticle Fermi surface of YPtBi can be probed through unique signatures in Fermiology (6). First, a splitting of the primary oscillation frequency into two components (39 T and 50 T) was understood as a signature of inner and outer orbits

Downloaded from https://www.pnas.org by UNIVERSITY OF MARYLAND; MCKELDIN LIBRARY on November 17, 2026 from IP address 129.2.89.183.

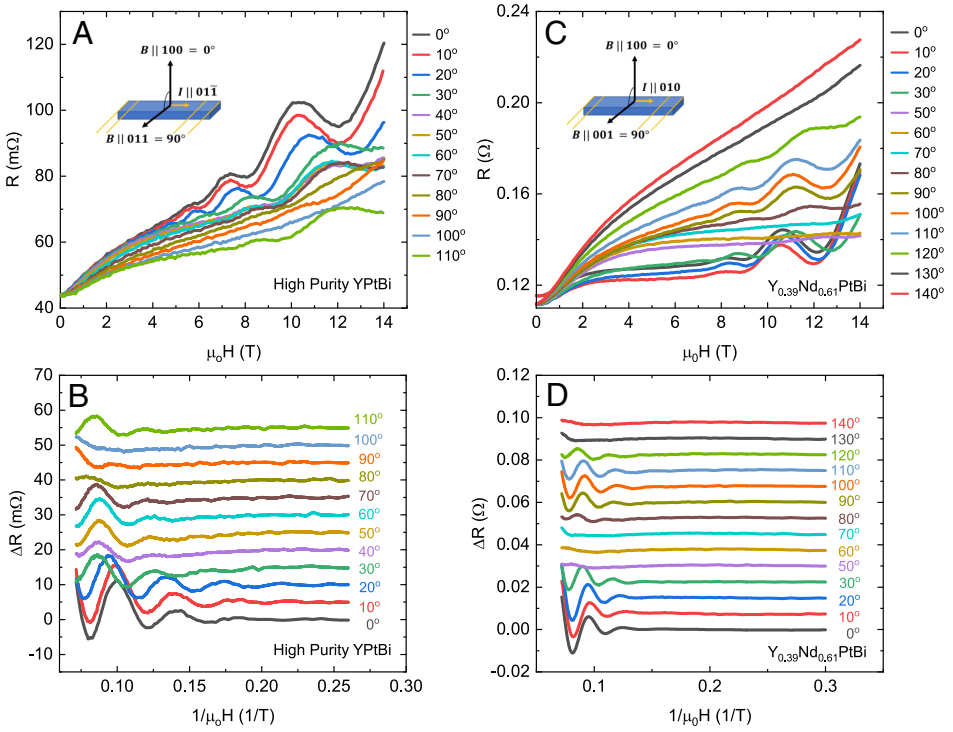


Fig. 3. Angle-dependent probe of $j = 3/2$ Fermi surface in YPtBi. Rotation measurements on the high purity and (Y,Nd)PtBi samples. Raw data and subtracted data offset to show the oscillations at various angles for the (*A, B*) high purity sample and (*C, D*) (Y,Nd)PtBi sample. The subtracted data clearly showing a suppression of amplitude around to 011 axis for both samples. Insets show the rotation axis of the field along the principal axes.

of spin-split Fermi surfaces due to the absence of parity symmetry (5). In our experiments, this effect has not been resolved, likely due to the limited field window in samples with larger Dingle factor, and the lower number of oscillation periods in the high purity case limiting our resolution.

Second, a notable and readily observed consequence of the $j = 3/2$ Fermi surface is a strong amplitude variation of oscillations in this otherwise isotropic system (6). As illustrated in Fig. 3, pronounced SdH oscillation amplitudes in both high purity YPtBi and (Y,Nd)PtBi show the expected strong angular variation as a function of transverse field rotation, with largest amplitude found for [100] orientation and strong suppression upon approach to the equivalent [110] direction in each case. FFT analysis confirms the frequency remains essentially constant through the amplitude change, consistent with prior work confirming the $j = 3/2$ Fermi surface.

With representative characterizations of disorder, purity, substitution, and doping effects on these samples, we now explore the impact on superconductivity in YPtBi. Across all sample types studied in this work, superconductivity remains exceptionally tolerant. Fig. 4 summarizes the robust nature of the superconducting transition to these perturbations, including little change in the resistive T_c, whether plotted as a function of sample type (Fig. 4*A*), residual resistivity (Fig. 4*C*) or carrier density changes (Fig. 4*D*). Through the combination of ultra-high purity, induced disorder, and hole-doping, this insensitivity spans a remarkable range of parameter space, from the lowest carrier densities ($\sim 10^{17}$ cm^{-3}) to the highest scattering rates ($\sim$5 mΩcm).

To confirm the bulk nature of superconductivity, we performed microwave cavity perturbation experiments on a high purity YPtBi sample. Fig. 4*B* plots the real and imaginary parts of the complex surface impedance $Z_s(T) = R_s(T) + iX_s(T)$ for a 7.07 GHz cavity mode. Both components are roughly constant for the displayed range of the normal state, and show a slight decrease preceding the superconducting transition at 980 mK where a kink can be seen in $R_s(T)$. The drops in $R_s(T)$ and $X_s(T)$ in the superconducting state indicate bulk screening. Note that unlike the dc resistivity (shown in Fig. 4*A*) the surface resistance does not show an abrupt drop to zero at T_c since this is a microwave frequency measurement where loss is expected in the superconducting state. There is, however, very large residual loss at zero-temperature, suggestive of the exotic nature of this material. Based on the minimum temperature surface reactance X_0, the zero-temperature penetration depth can be estimated as $\lambda_0 \approx (X_0/\mu_0\omega) \approx 10$ μm at this frequency. Note that this assumes the imaginary part of the complex conductivity is much larger than the real part deep in the superconducting state; however, this is almost certainly not the case here. A more detailed analysis results in an even larger value of the zero-temperature penetration depth $\lambda_0 \approx 14$ μm. Most of the sample is clearly participating in the Meissner state screening response with a relatively large (compared with other superconductors) layer of screening currents. Based on this, the scenario of filamentary channels of superconducting screening currents is unlikely.

This places strong constraints on the mechanism responsible for superconducting pairing in this material, in particular in the cases of nonmagnetic disorder and carrier doping. In conventional BCS superconductors with isotropic s-wave pairing, nonmagnetic disorder does not suppress superconductivity as a result of Anderson's theorem. However, in unconventional superconductors with a sign-changing gap structure, both magnetic and nonmagnetic disorder act as strong pair-breakers, leading to rapid suppression of T_c characterized by the Abrikosov-Gor'kov (AG) model (28, 29) The fact that superconductivity in YPtBi persists even in heavily disordered samples, where residual

Downloaded from https://www.pnas.org by UNIVERSITY OF MARYLAND; MCKELDIN LIBRARY on November 17, 2026 from IP address 129.2.89.183.

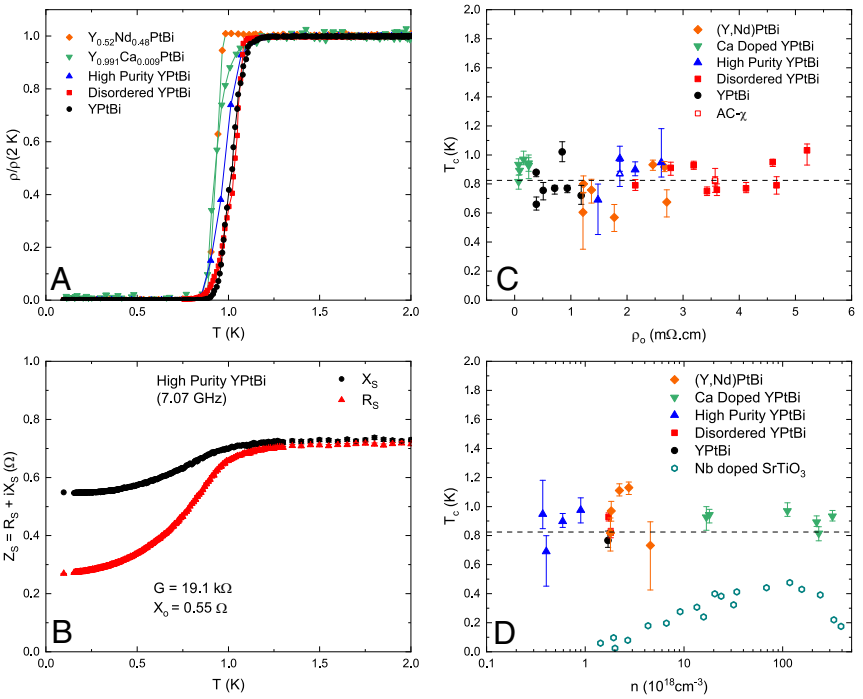


Fig. 4. Insensitivity of $j = 3/2$ superconductivity to disorder and carrier density tuning. (*A*) Normalized resistivity curves for the samples clearly showing no variation in transition temperature. (*B*) Microwave surface impedance Z_S of high purity YPtBi crystal vs. temperature with the surface resistance R_S in red and surface reactance X_S in black. (*C*) Various samples measured showing no change in T_c due to disorder. (*D*) T_c vs. carrier density showing no change in the transition temperature.

resistivity is strongly enhanced, suggests that the pairing state is either fully gapped and protected by symmetry, or rooted in an unconventional but disorder-resilient channel. One possibility is the presence of higher-angular momentum multicomponent order parameters such as quintet (J = 2) or septet (J = 3) pairing states, which can exhibit complex gap structures and in some cases robustness to certain types of disorder (24, 30–32).

The lack of sensitivity to carrier density is a more profound observation, challenging the applicability of a conventional electron–phonon mediated pairing mechanism which typically exhibits a strong dependence on the density of states and is sensitive to changes in band filling. For a conventional BCS superconductor, T_c is expected to increase with increasing carrier density (33). While a few counterexamples exist, such as unconventional dilute superconductors like Li-intercalated layered nitrides (34, 35), these are cases where T_c nevertheless shows a strong response to doping. However, the lack of T_c change over three orders of magnitude carrier density tuning (cf. Fig. 4*C*) is unprecedented. Even in the case of the dilute superconductor $SrTiO_3$, which has emerged as a canonical example of superconductivity at extremely low carrier densities (36, 37), there is a strong variation with doping that is evident in the comparison in Fig. 4*C*). The presence of superconductivity in both the dilute and heavily doped metallic regimes suggests that the pairing mechanism is not only robust but fundamentally distinct from any other known superconductor.

This behavior supports the idea that superconductivity in YPtBi is not tied to a fine-tuned Fermi surface instability or a high density of states at the Fermi level, but rather an alternative mechanism. In conventional pairing, T_c is primarily governed by the pairing amplitude and scales with the density of states at the Fermi level. In contrast, in the dilute limit where the Fermi energy becomes comparable to the pairing scale, superconductivity can enter a crossover regime in which fermion pairs form at temperatures well above the phase ordering temperatures and long range superconducting coherence is instead governed by superfluid phase stiffness $D_S \propto n_s/m^*$, where n_s is superfluid density and m^* is the effective mass. This scenario has been heavily studied in the cuprate superconductors (38), where the parallel increase of T_c and superfluid density in the underdoped regime is consistent with a phase ordering limited transition, while becoming insensitive to further increases in stiffness on the overdoped side (39). In particular, once the phase stiffness exceeds the minimum threshold required to establish global coherence, further increases in the n_s/m^* do not lead to enhancement of T_c, indicating a crossover from a stiffness limited to a pairing limited regime (40). While YPtBi is inherently distinct from the cuprates, this phenomenology provides an important precedent for interpreting a saturation of T_c in the presence of large changes in carrier density and Fermi surface volume.

Several aspects of YPtBi naturally place it near the crossover regime. The carrier densities of the undoped and high purity samples imply an extremely small Fermi energy, comparable to or moderately larger than the superconducting gap scale inferred from T_c. In this limit, coherence length is expected to be short and the size of the Cooper pairs can approach interparticle spacing, blurring the distinction between weakly bound Cooper pairs and tightly bound composite bosons. Similar physics has been extensively discussed in dilute superconductors and semimetals, most notably in $SrTiO_3$, which cannot be adequately described within weak coupling BCS theory and instead requires consideration of strong coupling, pairing fluctuations, and the separation between pair formation and phase coherence scales (41). In this system, superconductivity persists down to carrier densities as low as 10^{17} cm^{-3}, and the small Fermi energy places the system close to a BCS-BEC crossover regime in which phase coherence plays a central role in determining T_c (42). Although the microscopic pairing mechanism in $SrTiO_3$ differs from that

Downloaded from https://www.pnas.org by UNIVERSITY OF MARYLAND; MCKELDIN LIBRARY on November 17, 2026 from IP address 129.2.89.183.

in YPtBi, the underlying energetic hierarchy, small E_F, robust pairing and potentially phase stiffness-limited superconductivity, provides a useful and well established point of comparison.

Within this picture, T_c is not limited by pair formation but by the ability of the system to establish phase coherence. Notably, phase stiffness can be weakly sensitive to nonmagnetic disorder and only weakly dependent on the details of the Fermi surface, provided sufficient density of paired carriers exists. This provides a natural explanation for the striking insensitivity of T_c in YPtBi to disorder, carrier concentration, and even substantial changes to the Fermi surface volume by Ca doping.

Importantly, the phase stiffness perspective is not mutually exclusive with unconventional high spin pairing. On the contrary, pairing between $j = 3/2$ quasiparticles can naturally yield strong pairing amplitudes even at low carrier densities, while the resultant multicomponent order parameter might be relatively insensitive to impurity scattering. In this sense, YPtBi may represent a rare example where high angular momentum, spin–orbit-entangled pairing coexists with crossover physics typically associated with dilute superconductors, placing it in a regime where superconductivity is stabilized by robust pair formation but limited primarily by phase stiffness.

These findings establish YPtBi as a highly unusual superconductor where superconductivity is a remarkably robust ground state. The interplay between low carrier density, strong spin–orbit coupling, band inversion, and potentially phase stiffness limited coherence create a fertile ground for unconventional pairing. This work not only deepens our understanding of the complex relationship between electronic structure and superconductivity in YPtBi, but also provides a foundation for future theoretical and experimental studies aimed at uncovering the topological nature of its superconducting state.

Materials and Methods

Crystal Growth. YPtBi single crystals were grown using the molten Bi flux method. Y, Pt, and Bi in a molar ratio of 1:1:20 were placed in an alumina crucible and sealed in a quartz tube under an argon atmosphere. The excess Bi acts as a self-flux. The mixture was heated to 1,100 °C at a rate of 50 °C/h, held at that temperature for 12 h to ensure homogenization, and then slow-cooled to 520 °C at 3 °C/h before centrifuging to separate the crystals from the flux. Unless otherwise noted, measurements on these as-grown samples are represented by black circles or lines throughout this work.

High-purity crystals were grown using higher-purity starting materials: 99.99% Y, 99.999% Pt, and 99.9999% Bi at the Max Planck Institute for Chemical Physics of Solids. Standard-purity samples used 99.9% Y and Pt and 99.99% Bi. All purities stated are in metals basis. Measurements on these high-purity samples are represented by blue triangles or lines.

To introduce additional disorder without altering chemical composition, Au powder was added to the growth in varying quantities, up to a maximum of 20% relative to the Y molar amount. Elemental analysis via energy-dispersive spectroscopy (EDS) and wavelength-dispersive spectroscopy (WDS) showed no detectable Au in the crystals. Because these techniques are surface-sensitive, we also performed inductively coupled plasma (ICP) analysis, which dissolves the entire crystal to probe its bulk composition and has a sensitivity of parts per million (ppm). ICP confirmed the absence of Au, indicating that it is not chemically incorporated into the lattice. This suggests that Au acts solely as a source of disorder, introducing additional scattering centers without affecting the chemical potential. This conclusion is further supported by our electrical transport measurements. These disordered samples are indicated by red squares or lines in the figures.

Ca-doped samples were prepared by introducing Ca into the melt, in concentrations up to 50% relative to the Y molar amount. X-ray fluorescence (XRF) and EDS confirm the presence of Ca in the crystals, though the incorporated concentration is significantly lower than the nominal, reaching a maximum of ∼6%. Despite this, clear signatures of hole doping are observed in measurements of resistivity, Hall effect, and quantum oscillations. These Ca-doped samples are denoted by green triangles or lines throughout this work.

Nd-substituted samples were prepared by introducing Nd into the melt, in concentrations up to 50% relative to the Y molar amount. The concentration of Nd was confirmed by magnetic susceptibility measurements. These Nd substituted samples are denoted by green triangles or lines throughout this work.

Characterization. Powder X-ray diffraction (XRD) measurements on the samples confirm that they retain the YPtBi crystal structure, with diffraction peaks matching published data.

Resistivity Measurements. Electrical resistivity samples were prepared by polishing crystals into bar-shaped samples and attaching gold wire leads with silver paste, and subsequently measuring in a Quantum Design Physical Property Measurement System (PPMS) equipped with a 14T magnet for resistance and magnetoresistance measurements. To probe the superconducting state we used the adiabatic demagnetization refrigerator (ADR) insert with the PPMS, applying a field procedure (ramping to 2.5 T then zero) to cool samples to 100 mK by adiabatic demagnetization refrigeration. We measure the resistivity as the system warms up from 100 mK at zero field. High magnetic field measurements were done with a 41.5 T resistive magnet at the National High Magnetic Field Laboratory (NHMFL).

To investigate the strong anisotropy of oscillation amplitude due to the $j = 3/2$ electronic states in YPtBi, we carried out comprehensive angle-dependent quantum oscillation measurements in the high purity sample and Nd-substituted samples. Samples were first aligned with Laue X-ray diffraction to ensure precise crystallographic alignment. Following alignment, resistivity measurements were performed at 2 K under magnetic fields up to 14 T. The electrical current was applied along [011] crystallographic direction for the high purity sample and [010] axis for the Nd substituted samples. To systematically study the angular dependence, the magnetic field was rotated in discrete 10° increments. Throughout the rotation, the magnetic field was kept perpendicular to the current.

Microwave Measurements. We determine the surface impedance Z_S from microwave cavity perturbation experiments. A resonant cavity operating at frequencies between 2 and 12 GHz is perturbed by a sample (high purity YPtBi). Resonant modes of the cavity induce screening currents to flow on the sample's surface, probing the Meissner state electrodynamics of the sample. The surface impedance is related to the resonant frequency and quality factor by two constants unique to each mode: the geometry factor G (which relates the strength of the fields at the sample location to that of the rest of the cavity) and an offset for the surface reactance X_0. We determine these constants by comparing the resonance data in the normal state to the dc resistivity (43–45).

The microwave cavity perturbation experiments were performed in a Blue Fors dilution refrigerator (BF-XLD400) with the resonator attached to the cold plate, which keeps the resonant cavity at a nominal temperature of 100 mK, while the sample is suspended in the center of the cavity on a sapphire "hot finger" (43, 46–48) allowing the sample to be heated up to 10 K while remaining thermally isolated from the rest of cavity.

Data, Materials, and Software Availability. All study data are included in the article and/or *SI Appendix*.

ACKNOWLEDGMENTS. Research at the University of Maryland was supported by the Gordon and Betty Moore Foundation's Emergent Phenomena in Quantum Systems (EPiQS) Initiative Grant No. GBMF9071 (materials synthesis), the U.S. NSF Grant No. DMR2303090 (sample preparation), the Department of Energy, Office of Basic Energy Sciences Award No. DE-SC-0019154 (experimental measurements), the National Institute of Standards and Technology (NIST) Center for Neutron Research, and the Maryland Quantum Materials Center. The work by A.C.-J. and S.M.A. was funded by the US Department of Energy/High Energy Physics through Grant No. DESC0017931, and the Army Research Office under Grant Number ARO W911NF-24-1-0153. The research work at Max Planck Institute for Chemical Physics of Solids was financially supported by the Deutsche Forschungsgemeinschaft (DFG, German

Downloaded from https://www.pnas.org by UNIVERSITY OF MARYLAND; MCKELDIN LIBRARY on November 17, 2026 from IP address 129.2.89.183.

Research Foundation) through SFB 1143 (project ID 247310070), QUAST (project ID FOR 5249), the Würzburg-Dresden Cluster of Excellence ctd.qmat–Complexity, Topology and Dynamics in Quantum Matter (EXC 2147, project-id 390858490), and the European Union through Program Exchange for Chiral Symmetry (EXQIRAL) (No. 101131579).

Author affiliations: [a]Department of Physics, Maryland Quantum Materials Center, University of Maryland, College Park, MD 20742; [b]Department of Physics, Missouri University of Science and Technology, Rolla, MO 65409; [c]Department of Chemistry and Biochemistry, University of Maryland, College Park, MD 20742; [d]National High Magnetic Field Laboratory, Tallahassee, FL 32310; [e]Max Planck Institute for Chemical Physics of Solids, Dresden 01187, Germany; and [f]Canadian Institute for Advanced Research, Toronto, ON M5G 1Z8, Canada

1. S. Chadov *et al*., Tunable multifunctional topological insulators in ternary Heusler compounds. *Nat. Mater.* **9**, 541–545 (2010).
2. H. Lin *et al*., Half-Heusler ternary compounds as new multifunctional experimental platforms for topological quantum phenomena. *Nat. Mater.* **9**, 546–549 (2010).
3. D. Xiao *et al*., Half-Heusler compounds as a new class of three-dimensional topological insulators. *Phys. Rev. Lett.* **105**, 096404 (2010).
4. N. P. Butch, P. Syers, K. Kirshenbaum, A. P. Hope, J. Paglione, Superconductivity in the topological semimetal YPtBi. *Phys. Rev. B* **84**, 220504 (2011).
5. H. Kim *et al*., Beyond triplet: Unconventional superconductivity in a spin-3/2 topological semimetal. *Sci. Adv.* **4**, eaao4513 (2018).
6. H. Kim *et al*., Quantum oscillations of the $j = 3/2$ fermi surface in the topological semimetal YPtBi. *Phys. Rev. Res.* **4**, 033169 (2022).
7. M. Meinert, Unconventional superconductivity in YPtBi and related topological semimetals. *Phys. Rev. Lett.* **116**, 137001 (2016).
8. X. Lin, Z. Zhu, B. Fauqué, K. Behnia, Fermi surface of the most dilute superconductor. *Phys. Rev. X* **3**, 021002 (2013).
9. P. M. R. Brydon, L. Wang, M. Weinert, D. F. Agterberg, Pairing of $j = 3/2$ fermions in half-Heusler superconductors. *Phys. Rev. Lett.* **116**, 177001 (2016).
10. J. Yu, C. X. Liu, Singlet-quintet mixing in spin-orbit coupled superconductors with $j = \frac{3}{2}$ fermions. *Phys. Rev. B* **98**, 104514 (2018).
11. L. Savary, J. Ruhman, J. W. F. Venderbos, L. Fu, P. A. Lee, Superconductivity in three-dimensional spin-orbit coupled semimetals. *Phys. Rev. B* **96**, 214514 (2017).
12. H. Kim *et al*., Campbell penetration depth in low carrier density superconductor YPtBi. *Phys. Rev. B* **104**, 014510 (2021).
13. B. Roy, S. A. A. Ghorashi, M. S. Foster, A. H. Nevidomskyy, Topological superconductivity of spin-3/2 carriers in a three-dimensional doped luttinger semimetal. *Phys. Rev. B* **99**, 054505 (2019a).
14. J. W. F. Venderbos, L. Savary, J. Ruhman, P. A. Lee, L. Fu, Pairing states of spin-$\frac{3}{2}$ fermions: Symmetry-enforced topological gap functions. *Phys. Rev. X* **8**, 011029 (2018).
15. W. Yang, T. Xiang, C. Wu, Majorana surface modes of nodal topological pairings in spin-$\frac{3}{2}$ semimetals. *Phys. Rev. B* **96**, 144514 (2017).
16. C. Timm, A. P. Schnyder, D. F. Agterberg, P. M. R. Brydon, Inflated nodes and surface states in superconducting half-Heusler compounds. *Phys. Rev. B* **96**, 094526 (2017).
17. G. Sim *et al*., Topological $d + s$ wave superconductors in a multiorbital quadratic band touching system. *Phys. Rev. B* **100**, 064509 (2019).
18. T. Suzuki *et al*., Large anomalous hall effect in a half-Heusler antiferromagnet. *Nat. Phys.* **12**, 1119–1123 (2016).
19. M. Hirschberger *et al*., The chiral anomaly and thermopower of Weyl fermions in the half-Heusler gdptbi. *Nat. Mater.* **15**, 1161–1165 (2016).
20. K. Manna, Y. Sun, L. Muechler, J. Kübler, C. Felser, Heusler, Weyl and berry. *Nat. Rev. Mater.* **3**, 244–256 (2018).
21. B. Roy, S. A. A. Ghorashi, M. S. Foster, A. H. Nevidomskyy, Topological superconductivity of spin-3/2 carriers in a three-dimensional doped luttinger semimetal. *Phys. Rev. B* **99**, 054505 (2019b).
22. A. L. Szabó, R. Moessner, B. Roy, Interacting spin-$\frac{3}{2}$ fermions in a luttinger semimetal: Competing phases and their selection in the global phase diagram. *Phys. Rev. B* **103**, 165139 (2021).
23. S. Kobayashi, A. Bhattacharya, C. Timm, P. M. R. Brydon, Bogoliubov fermi surfaces from pairing of emergent $j = \frac{3}{2}$ fermions on the pyrochlore lattice. *Phys. Rev. B* **105**, 134507 (2022).
24. J. Yu, C. X. Liu, Spin susceptibility, upper critical field, and disorder effect in $j = 3/2$ superconductors with singlet-quintet mixing. *J. Appl. Phys.* **128**, 063904 (2020).
25. D. Kim, T. Sato, S. Kobayashi, Y. Asano, Spin susceptibility of a $j = 3/2$ superconductor. *J. Phys. Soc. Jpn.* **92**, 054703 (2023).
26. E. Persky *et al*., Possible unconventional surface superconductivity in the half-Heusler compound YPtBi. *Phys. Rev. B* **111**, 245417 (2025).
27. D. Shoenberg, *Magnetic Oscillations in Metals* (Cambridge University Press, London, 2009).
28. A. Abrikosov, L. Gor'kov, Contribution to the theory of superconducting alloys with paramagnetic impurities. *JETP* **12**, 1243–1253 (1961).
29. I. La, Vector pairing in superconductors of small dimensions. *JETP Lett.* **2**, 130–132 (1965).
30. D. C. Cavanagh, P. M. R. Brydon, Robustness of unconventional *s*-wave superconducting states against disorder. *Phys. Rev. B* **101**, 054509 (2020).
31. M. Bahari, S. B. Zhang, B. Trauzettel, Intrinsic finite-energy cooper pairing in $j = 3/2$ superconductors. *Phys. Rev. Res.* **4**, L012017 (2022).
32. P. Dutta, F. Parhizgar, A. M. Black-Schaffer, Superconductivity in spin-3/2 systems: Symmetry classification, odd-frequency pairs, and bogoliubov fermi surfaces. *Phys. Rev. Res.* **3**, 033255 (2021).
33. M. Tinkham, *Introduction to Superconductivity* (Dover Publications, North Chelmsford, MA, ed. 2, 2004).
34. Y. Taguchi, A. Kitora, Y. Iwasa, Increase in T_c upon reduction of doping in Li_xZrNCl superconductors. *Phys. Rev. Lett.* **97**, 107001 (2006).
35. Y. Nakagawa *et al*., Gate-controlled low carrier density superconductors: Toward the two-dimensional BCS-BEC crossover. *Phys. Rev. B* **98**, 064512 (2018).
36. P. Nozières, S. Schmitt-Rink, Bose condensation in an attractive fermion gas: From weak to strong coupling superconductivity. *J. Low Temp. Phys.* **59**, 195–211 (1985).
37. D. M. Eagles, Possible pairing without superconductivity at low carrier concentrations in bulk and thin-film superconducting semiconductors. *Phys. Rev.* **186**, 456–463 (1969).
38. V. J. Emery, S. A. Kivelson, Importance of phase fluctuations in superconductors with small superfluid density. *Nature* **374**, 434–437 (1995).
39. Y. J. Uemura *et al*., Universal correlations between T_c and $\frac{n_s}{m^*}$ (carrier density over effective mass) in high-T_c cuprate superconductors. *Phys. Rev. Lett.* **62**, 2317–2320 (1989).
40. S. Kivelson, Making high tc higher: A theoretical proposal. *Phys. B Condens. Matter* **318**, 61–67 (2002).
41. M. N. Gastiasoro, J. Ruhman, R. M. Fernandes, Superconductivity in dilute srtio3: A review. *Ann. Phys.* **417**, 168107 (2020).
42. Q. Chen, Z. Wang, R. Boyack, S. Yang, K. Levin, When superconductivity crosses over: From BCS to BEC. *Rev. Mod. Phys.* **96**, 025002 (2024).
43. J. Mao, D. H. Wu, J. L. Peng, R. L. Greene, S. M. Anlage, Anisotropic surface impedance of $YBa_2Cu_3O_{7-\delta}$ single crystals. *Phys. Rev. B* **51**, 3316(R)–3319(R) (1995).
44. S. Bae *et al*., Anomalous normal fluid response in a chiral superconductor UTe_2. *Nat. Commun.* **12**, 2644 (2021).
45. A. Carlton-Jones *et al*., Revealing isotropic abundant low-energy excitations in UTe_2 through complex microwave surface impedance. *Phys. Rev. B* **112**, 014519 (2025).
46. S. Sridhar, W. L. Kennedy, Novel technique to measure the microwave response of high T_c superconductors between 4.2 and 200 K. *Rev. Sci. Instrum.* **59**, 531–536 (1988).
47. D. L. Rubin *et al*., Observation of a narrow superconducting transition at 6 GHz in crystals of $YBa_2Cu_3O_7$. *Phys. Rev. B* **38**, 6538–6542 (1988).
48. M. Trunin, Temperature dependence of microwave surface impedance in high-T_c single crystals: Experimental and theoretical aspects. *J. Supercond.* **11**, 381–408 (1998).

Downloaded from https://www.pnas.org by UNIVERSITY OF MARYLAND; MCKELDIN LIBRARY on November 17, 2026 from IP address 129.2.89.183.

PNAS

Supporting Information for

Resilient j=3/2 superconductivity in topological semimetal YPtBi

Prathum Saraf, Nicholas A. Crombie, Rahul Sharma, Jared Z. Dans, Danila Sokratov, Carsyn L. Mueller, Ram Kumar, Hyunsoo Kim, Connor Roncaioli, Winslow Weiss, Arthur Carlton-Jones, Peter Y. Zavalij, Steven M. Anlage, David Graf, Chandra Shekhar, Claudia Felser, Johnpierre Paglione

Johnpierre Paglione and Claudia Felser
E-mail: paglione@umd.edu or claudia.felser@cpfs.mpg.de

This PDF file includes:

Figs. S1 to S5
Tables S1 to S6

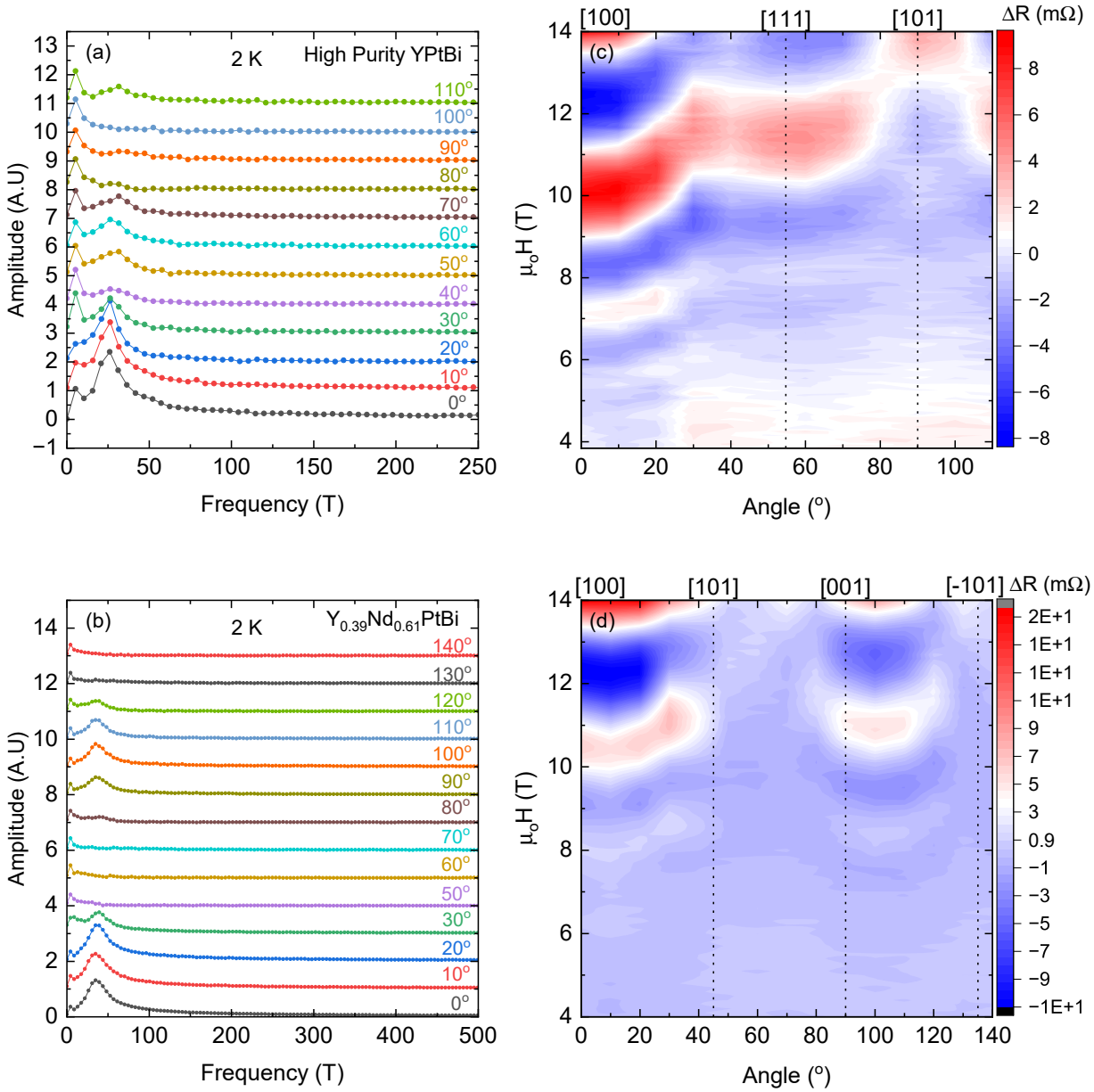


Fig. S1. (a,b) FFT analysis of High purity and Nd substituted samples showing no change in oscillation frequency with angle indicating a spherical Fermi surface. (c,d) Amplitude suppression seen along [110] type axis.

Single Crystal X-ray result for Disordered YPtBi. Due to just one electron difference between Pt and Au, it is not possible to determine the ratio between the two. We refined only Y occupation faction and Pt and Au as complementary to 100%. Pt:Au occupations were kept fixed at 85:15 which was the nominal ratio.

Table S1. Single Crystal X-ray result for Disordered YPtBi

Empirical formula	$Y_{1.07}Au_{0.14}Pt_{0.79}Bi$
Formula weight	486.08
Temperature/K	240(2)
Crystal system	cubic
Space group	Fm-3m
a/Å	6.6505(6)
b/Å	6.6505(6)
c/Å	6.6505(6)
$\alpha/^\circ$	90
$\beta/^\circ$	90
$\gamma/^\circ$	90
Volume/Å^3	294.15(8)
Z	4
ρ_{calc} g/cm^3	10.976
μ/mm^{-1}	124.774
F(000)	790.0
Crystal Size/mm^3	0.05 $\times$ 0.025 $\times$ 0.005
Radiation	MoKα (λ = 0.71073)
2θ range for data collection/$^\circ$	10.62 to 61.292
Index ranges	-9 $\leq$ h $\leq$ 9, -9 $\leq$ k $\leq$ 9, -9 $\leq$ l $\leq$ 9
Reflections collected	1443
Independent reflections	40 [R_{int} = 0.0552, R_{sigma} = 0.0178]
Data/restraints/parameters	40/0/5
Goodness-of-fit on F^2	1.225
Final R indexes [I >= 2σ(I)]	R_1 = 0.0205, wR_2 = 0.0449
Final R indexes [all data]	R_1 = 0.0205, wR_2 = 0.0449
Largest diff. peak/hole / eÅ^{-3}	2.05/-1.65

Prafulla Saraf, Nicholas A. Crombie, Rahul Sharma, Jared Z. Dans, Danila Sokratov, Carsyn L. Mueller, Ram Kumar, Hyunsoo Kim, Connor Roncaioli, Winslow Weiss, Arthur Carlton-Jones, Peter Y. Zavalij, Steven M. Anlage, David Graf, Chandra Shekhar, Claudia Felser, Johnpierre Paglione

Table S2. Single Crystal X-ray result for YPtBi

Empirical formula	YPtBi
Formula weight	492.98
Temperature/K	250(2)
Crystal system	cubic
Space group	Fm-3m
a/Å	6.6522(10)
b/Å	6.6522(10)
c/Å	6.6522(10)
$\alpha/^\circ$	90
$\beta/^\circ$	90
$\gamma/^\circ$	90
Volume/Å^3	294.37(8)
Z	4
ρ_{calc} g/cm^3	11.124
μ/mm^{-1}	126.235
F(000)	800
Crystal Size/mm^3	0.08 $\times$ 0.08 $\times$ 0.14
Radiation	MoKα (λ = 0.71073)
2θ range for data collection/$^\circ$	10.62 to 61.292
Index ranges	-9 $\leq$ h $\leq$ 9, -9 $\leq$ k $\leq$ 9, -9 $\leq$ l $\leq$ 9
Reflections collected	1470
Independent reflections	68 [R$_{int}$ = 0.0342]
Data/restraints/parameters	68/0/5
Goodness-of-fit on F^2	1.000
Final R indexes [I >= 2σ(I)]	R$_1$ = 0.0127, wR$_2$ = 0.0320
Final R indexes [all data]	R$_1$ = 0.0127, wR$_2$ = 0.0320
Largest diff. peak/hole / eÅ^{-3}	1.376/-1.567

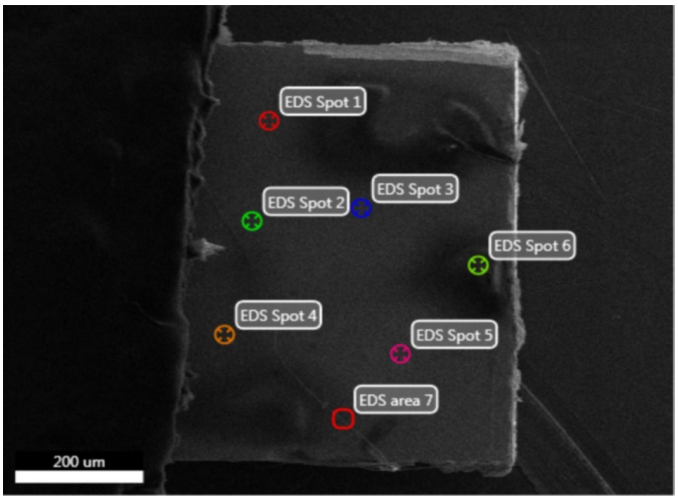


Fig. S2. Crystal picture for EDS data for $Y_{0.19}Nd_{0.81}PtBi$

Pratikshya Saraf, Nicholas A. Crombie, Rahul Sharma, Jared Z. Dans, Danila Sokratov, Carsyn L. Mueller, Ram Kumar, Hyunsoo Kim, Connor Roncaioli, Winslow Weiss, Arthur Carlton-Jones, Peter Y. Zavalij, Steven M. Anlage, David Graf, Chandra Shekhar, Claudia Felser, Johnpierre Paglione

Table S3. EDS data for $Y_{0.19}Nd_{0.81}PtBi$

	Y (atomic %)	Nd (atomic %)	Pt (atomic %)	Bi (atomic %)
Spot 1	8.08	3.23	32.35	34.43
Spot 2	8.15	4.90	30.65	33.51
Spot 3	7.98	4.34	30.43	34.94
Spot 4	7.67	3.99	29.78	36.20
Spot 5	6.59	9.19	31.39	36.75
Spot 6	6.92	2.40	31.39	36.75
Average	7.57	31.76	29.31	31.37

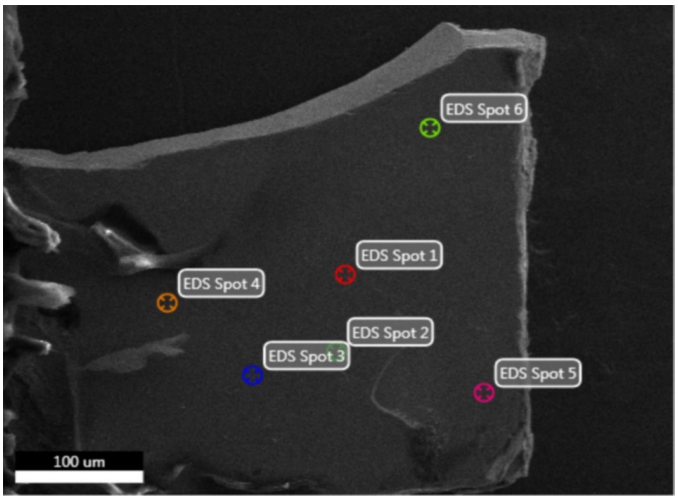


Fig. S3. Crystal picture for EDS data for $Y_{0.86}Nd_{0.14}PtBi$

Table S4. EDS data for $Y_{0.86}Nd_{0.14}PtBi$

	Y (atomic %)	Nd (atomic %)	Pt (atomic %)	Bi (atomic %)
Spot 1	29.99	3.23	32.35	34.43
Spot 2	30.94	4.90	30.65	33.51
Spot 3	30.28	4.34	30.43	34.94
Spot 4	30.03	3.99	29.78	36.20
Spot 5	26.16	9.19	31.39	36.75
Spot 6	29.46	2.40	31.39	36.75
Average	29.48	4.68	30.91	34.93

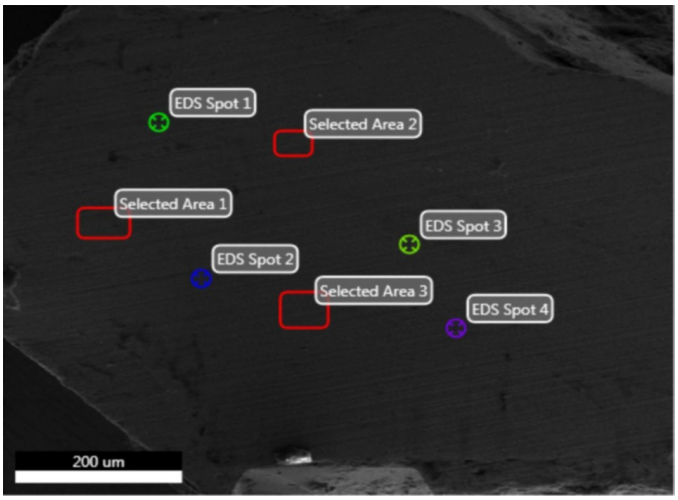


Fig. S4. Crystal picture for EDS data for $Y_{0.97}Ca_{0.03}PtBi$

Table S5. EDS data for $Y_{0.97}Ca_{0.03}PtBi$

	Y (atomic %)	Ca (atomic %)	Pt (atomic %)	Bi (atomic %)
Area 1	32.99	0.69	38.51	27.80
Area 2	32.51	0.96	38.74	27.79
Area 3	32.96	1.07	38.03	27.93
Area 4	32.68	1.72	37.77	27.83
Spot 2	31.74	0.98	36.51	29.77
Spot 3	33.01	0.35	37.81	28.83
Average	32.76	0.88	38.22	28.14

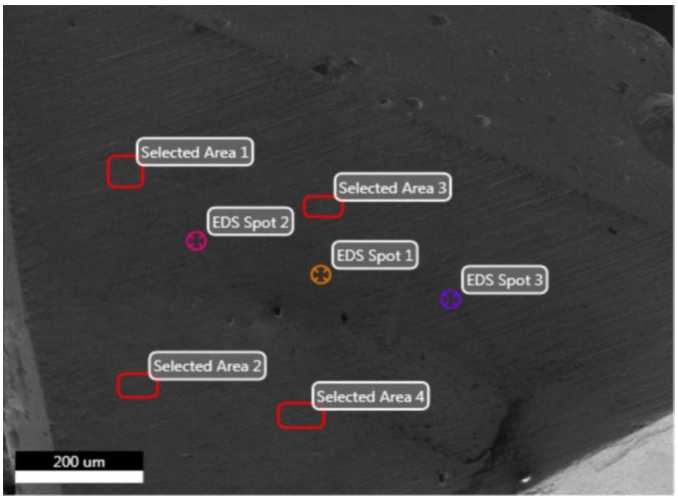


Fig. S5. Crystal picture for EDS data for $Y_{0.974}Ca_{0.026}PtBi$

Table S6. EDS data for $Y_{0.974}Ca_{0.026}PtBi$

	Y (atomic %)	Ca (atomic %)	Pt (atomic %)	Bi (atomic %)
Area 1	33.05	0.98	38.15	35.81
Area 2	32.73	1.13	38.34	27.79
Area 3	32.56	1.51	38.26	27.67
Spot 1	32.40	1.21	38.70	27.69
Spot 2	31.96	0.16	39.52	28.36
Spot 3	32.33	0.97	38.20	28.50
Spot 4	39.71	1.51	30.62	28.17
Average	33.53	1.07	37.40	29.14